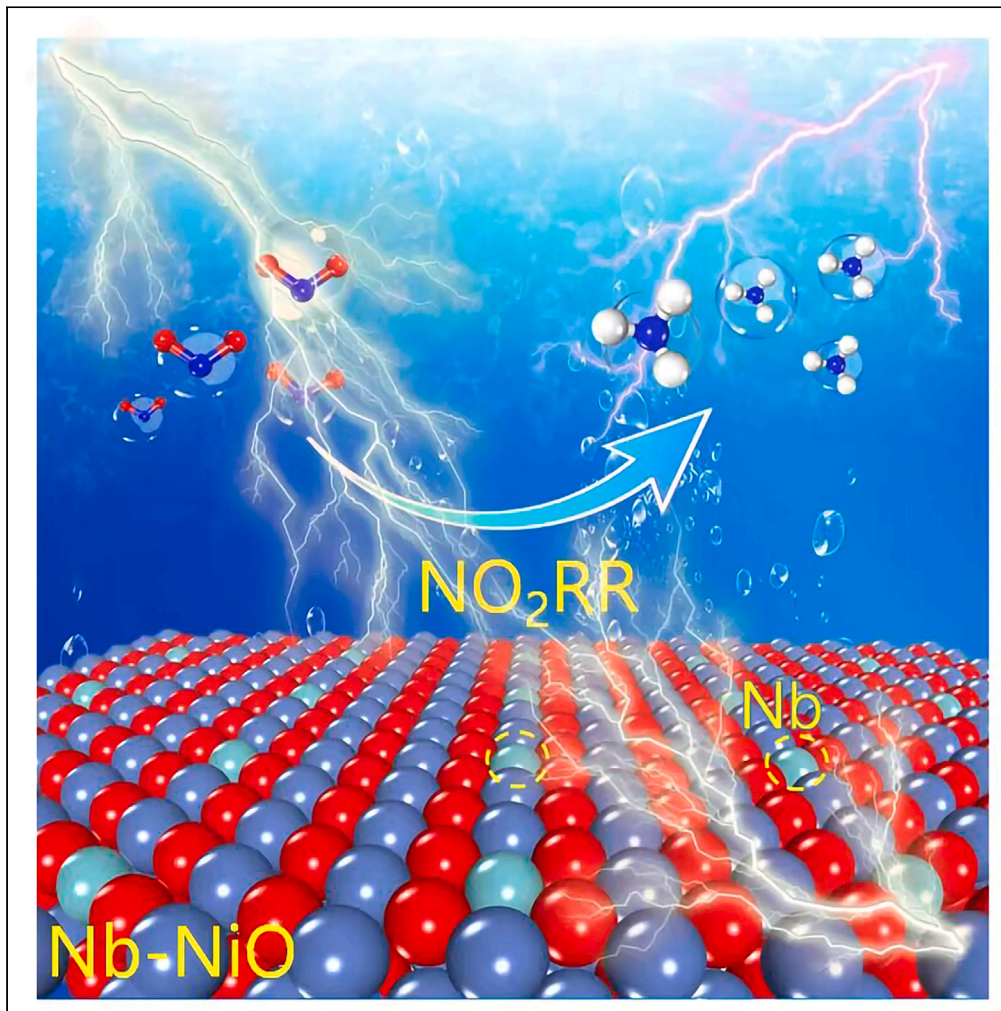


Article

Nb-doped NiO nanoflowers for nitrite electroreduction to ammonia



Ying Zhang, Yuying Wan, Xiaoxu Liu, Kai Chen, Ke Chu

chuk630@mail.lzjtu.cn

Highlights

Nb-doped NiO (Nb-NiO) is explored for electrochemical NO_2^- -to- NH_3 reduction (NO_2RR)

Nb-NiO exhibits the FE_{NH_3} of 92.4% with an NH_3 yield rate of $200.5 \mu\text{mol h}^{-1} \text{cm}^{-2}$

Nb-NiO can promote the NO_2^- activation and decrease the protonation energy barriers

Zhang et al., iScience 26, 107944
October 20, 2023 © 2023 The Author(s).
<https://doi.org/10.1016/j.isci.2023.107944>



Article

Nb-doped NiO nanoflowers for nitrite electroreduction to ammonia

Ying Zhang,^{1,3} Yuying Wan,^{1,3} Xiaoxu Liu,² Kai Chen,¹ and Ke Chu^{1,4,*}

SUMMARY

Electrocatalytic reduction of nitrite to ammonia (NO_2RR) is considered as an appealing route to simultaneously achieve sustainable ammonia production and abate hazardous nitrite pollution. Herein, atomically Nb-doped NiO nanoflowers are designed as a high-performance NO_2RR catalyst, which exhibits the highest NH_3 -Faradaic efficiency of 92.4% with an NH_3 yield rate of $200.5 \mu\text{mol h}^{-1} \text{cm}^{-2}$ at -0.6 V RHE . Theoretical calculations unravel that Nb dopants can act as Lewis acid sites to render effective NO_2^- activation, decreased protonation energy barriers, and restricted hydrogen evolution, ultimately leading to a high NO_2RR selectivity and activity.

INTRODUCTION

Ammonia (NH_3) serves as a crucial chemical for fertilizer production and also as a storage medium for renewable energy.^{1–3} Electrochemical N_2 -to- NH_3 reduction (NRR) in aqueous media is regarded as a prospective method for green NH_3 production,⁴ but the NRR remains far from practical application, arising from the high dissociation energy of $\text{N}\equiv\text{N}$ bond (927 kJ mol^{-1}), the competitive hydrogen evolution reaction (HER), and the low N_2 solubility.^{5–10} Nitrite (NO_2^-), a widespread N– pollutant, is extremely harmful to human health and ecological environment.^{11–14} Since NO_2^- possesses a weaker $\text{N}=\text{O}$ bond dissociation energy (204 kJ mol^{-1}) and a higher water solubility, electrocatalytic NO_2^- -to- NH_3 reduction (NO_2RR) via a direct six-electron transfer process is considered as an attractive approach to simultaneously achieve effective ammonia production and abate hazardous nitrite pollution.^{15–19} However, developing NO_2RR catalysts with high selectivity and activity remains a grand challenge.

As electron-deficient centers, Lewis acid sites possess empty orbitals capable of interacting with the electron lone pair of Lewis base NO_2^- species,²⁰ facilitating the activation and dissociation of NO_2^- . Besides, owing to the strong electrostatic repulsion effect, the adsorption of H atoms can be effectively impeded on Lewis acid sites,²¹ leading to an inhibited HER process. Therefore, the construction of Lewis acid sites on catalysts offers an efficient method for potentially achieving active and selective NO_2RR . Extensive research has indicated that incorporating metal dopants into transition metal oxides is an effective method to create Lewis acid sites because their strong electronic interactions lead to charge redistribution on different metal atoms.^{20–25} Particularly, when metal dopants exist in isolated single-atom form, abundant Lewis acid sites would be generated,^{26–28} which are greatly favorable for the maximized Lewis acidity and largely expedited NO_2RR activity.

Nb is known to possess a prominent Lewis acidity due to the existence of holes in its d orbitals.²⁹ Nb-based catalysts have also been demonstrated to show high catalytic activity in N-cycle electrocatalytic reactions toward the ammonia electrosynthesis.^{30–32} Therefore, in this work, atomically Nb doped in NiO (Nb–NiO) nanoflowers are designed as a high-performance NO_2RR catalyst, which exhibits a fascinating NO_2RR performance with the highest FENH₃ of 92.4% and NH_3 yield rate of $200.5 \mu\text{mol h}^{-1} \text{cm}^{-2}$ at -0.6 V , outperforming pristine NiO and many other reported NO_2RR catalysts. Theoretical calculations reveal the pivotal role of Lewis acid Nb dopants in facilitating the activity and selectivity of NO_2RR process.

RESULTS AND DISCUSSION

The synthesis of Nb–NiO nanoflowers is conducted by the combined hydrothermal and calcination methods (Figure 1A). The X-ray diffraction (XRD) patterns of both pristine NiO and Nb–NiO (Figure 1B) show the characteristic diffraction peaks of cubic NiO (No. 78–0643).³³ A detailed inspection reveals that Nb–NiO delivers a slightly lower peak intensity and wider full width at half maximum compared to pristine NiO, arising from the incorporation of Nb dopants in Nb–NiO (Figure S1). Representative scanning electron microscopy (SEM) (Figures 1C and 1D) image of Nb–NiO shows a typical nanoflower structure comprising many vertically aligned nanosheets, similar to that of original NiO (Figure S2A). The thin nanosheet feature of Nb–NiO (Figure 1E) and NiO (Figure S2B) can be further revealed by the transmission electron microscopy (TEM) image showing clear wrinkles and corrugations. In addition, the high-resolution transmission electron microscopy (HRTEM)

¹School of Materials Science and Engineering, Lanzhou Jiaotong University, Lanzhou 730070, China

²College of Science, Hebei North University, Zhangjiakou, Hebei 075000, China

³These authors contributed equally

⁴Lead contact

*Correspondence: chuk630@mail.lzjtu.cn

<https://doi.org/10.1016/j.isci.2023.107944>



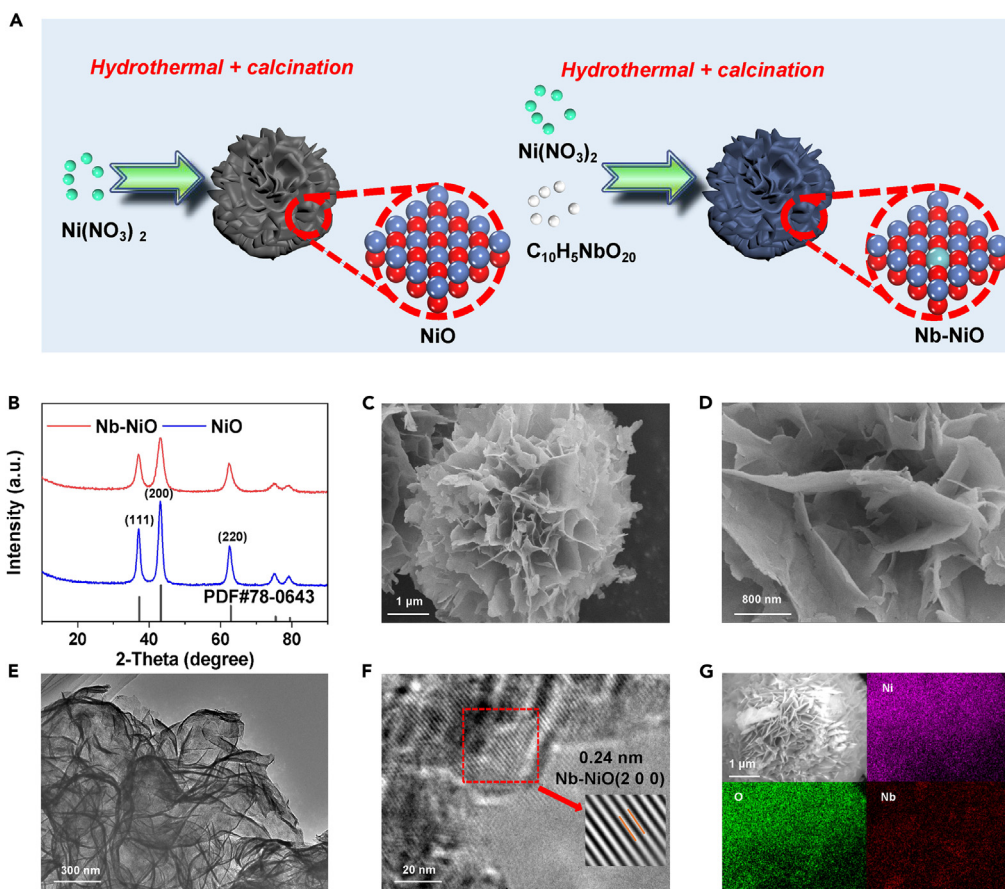


Figure 1. Morphology characteristics of $\text{Nb}-\text{NiO}$

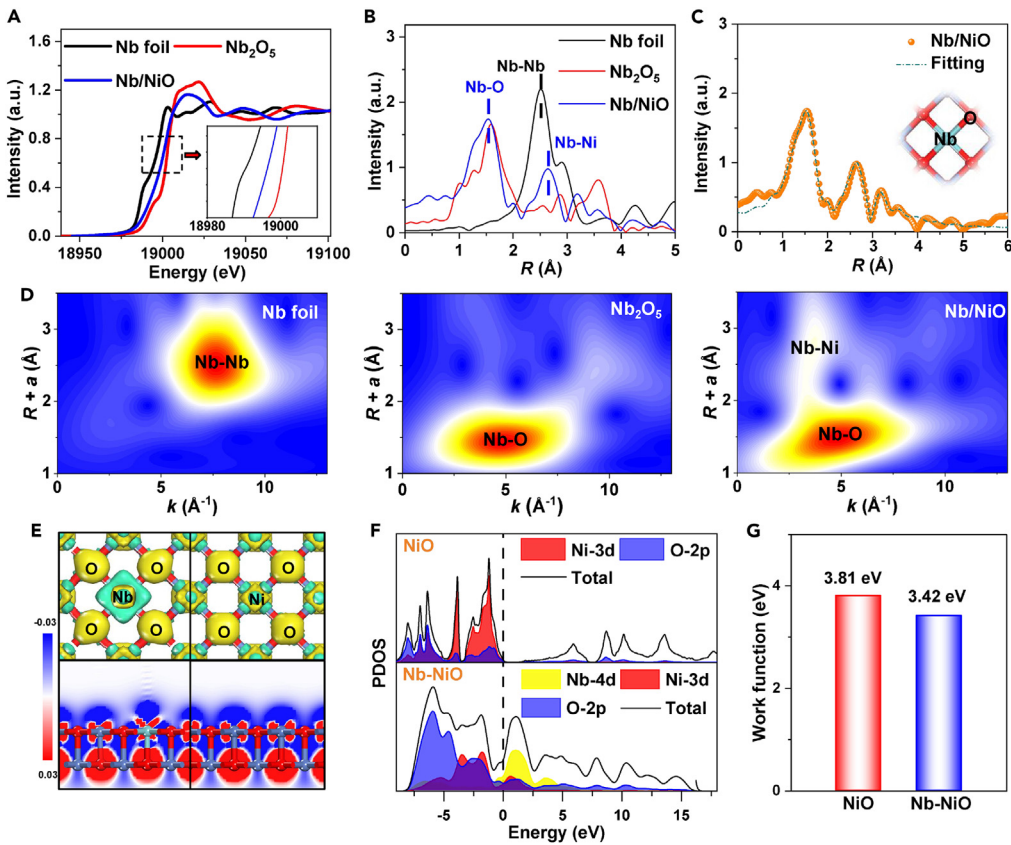
(A) Schematic diagram of the preparation route of NiO and $\text{Nb}-\text{NiO}$.

(B–G) Characterizations of as-prepared $\text{Nb}-\text{NiO}$: (B) XRD patterns, (C and D) SEM images, (E) TEM image, (F) HRTEM image, (G) Elemental mapping images.

image exhibits a clear lattice fringe of 0.24 nm, correlating well with (200) crystallographic plane of cubic NiO (Figure 1F). Elemental mapping images (Figure 1G) unveil that Nb dopants are uniformly dispersed over the whole surface of $\text{Nb}-\text{NiO}$ nanoflowers.

The X-ray absorption spectroscopy (XAS) characterizations are conducted to evaluate the coordination environment of $\text{Nb}-\text{NiO}$. The Nb K-edge X-ray absorption near edge structure (XANES) spectra (Figure 2A) show that the absorption edge of $\text{Nb}-\text{NiO}$ is situated between Nb foil and Nb_2O_5 , indicating that Nb dopants are in oxidation state. Linear XANES fitting result reveals that the average Nb valence state is +3.4 (Figure S3). The Nb K-edge extended X-ray absorption fine-structure (EXAFS) spectrum of $\text{Nb}-\text{NiO}$ (Figure 2B) reveals a dominant peak at 1.54 Å, which is assigned to Nb–O first coordination shell. The absence of Ni–Ni coordination bond confirms the automatically dispersed Nb dopants in $\text{Nb}-\text{NiO}$.^{34–36} Besides, the 2.65 Å peak is assigned to Nb–Ni second coordination shell. Similarly, the wavelet-transformed (WT, Figure 2D) profiles display that $\text{Nb}-\text{NiO}$ exhibits two Nb–O and Nb–Ni intensity maxima. EXAFS fitting analysis shows that the isolated Nb atom coordinates with five adjacent O atoms to form geometric Nb_1-O_5 moiety (Figure 2C; Table S1).

Density functional theory (DFT) computations are performed to investigate the electronic structures of $\text{Nb}-\text{NiO}$. On the basis of XRD and HRTEM results, we select (200) plane of NiO slab for $\text{Nb}-\text{NiO}$ structural modeling. As seen in Figure S4, by substituting a surface-exposed Ni atom with an Nb dopant, the resulting $\text{Nb}-\text{NiO}$ shows a rather negative formation energy of -2.46 eV, suggesting that Nb dopant incorporated in NiO lattice is thermodynamically feasible.³⁷ Charge density difference and electron location function (ELF, Figure 2E) maps of $\text{Nb}-\text{NiO}$ exhibit the noticeable electron-deficient regions around Nb dopant. This can be further verified by the detailed charge analysis (Figure S5), in which Nb dopant (+1.12 |e|) is more positively charged than Ni (+0.77 |e|) and thus Nb dopants can serve as Lewis acid sites to activate and polarize NO_2^- during the NO_2RR process.³⁸ The projected density of states (PDOS, Figure 2F) analysis displays that NiO possesses a distinct band gap, indicating its semiconducting nature. In stark contrast, introducing Nb dopant in NiO generates significant electronic states crossing the Fermi level, suggesting the metallic character and improved conductivity of $\text{Nb}-\text{NiO}$.³⁹ Meanwhile, as shown in Figure 2G (Figure S6), the calculated work function (Φ) value of $\text{Nb}-\text{NiO}$ is 3.42 eV, which is lower than that of NiO (3.81 eV). Thus, the proton-coupled electron transfer process and the electrocatalytic NO_2RR kinetics can be significantly facilitated on $\text{Nb}-\text{NiO}$.⁴⁰ Moreover, AIMD simulations of $\text{Nb}-\text{NiO}$ display the equilibrium states of energy and temperature (Figure S7), signifying the high thermodynamic stability of $\text{Nb}-\text{NiO}$.⁴⁰

**Figure 2. Structural characteristics of Nb–NiO**

(A, B, and D) (A) Nb K-edge XANES, (B) EXAFS spectra, and (D) WT profiles of Nb–NiO, Nb foil and Nb₂O₅. (C) EXAFS fitting analysis of Nb–NiO.

(E) Charge density difference (top half) and electron location function (bottom half), yellow and red: charge accumulation, cyan and blue: charge depletion. (F and G) (F) PDOS profiles and (G) calculated work functions of NiO and Nb–NiO.

Electrochemical NO₂RR performance of Nb–NiO is evaluated in 0.5 M Na₂SO₄ + 0.1 M NaNO₂ solution using an H cell based on a standard procedure flow chart (Figure S8).¹⁴ The produced liquid and gas products after NO₂RR electrolysis are determined by colorimetric and gas chromatography methods (Figures S9–S11),^{41–44} respectively. The linear sweep voltammetry (LSV) curves of Nb–NiO are measured firstly (Figure 3A), and a significant increase in current density (j) is observed for NO₂[−]-containing electrolyte compared to NO₂[−]-free electrolyte, signifying the high NO₂RR activity of Nb–NiO. Subsequently, the NO₂RR performance of Nb–NiO is quantitatively evaluated at various potentials using the combined chronoamperometry (Figure 3B) and colorimetric tests. Figure 3C shows that Nb–NiO shows a maximum FENH₃ of 92.4% at −0.6 V, with the corresponding NH₃ yield rate reaching 200.5 μmol h^{−1} cm^{−2}. Such NO₂RR performance is better than that of most reported NO₂RR catalysts as depicted in Figure 3D and Table S2. The controlled colorimetric measurements (Figure S12) and alternating experiments (Figure S13) attest that the generated NH₃ is derived from the NO₂RR electrolysis on Nb–NiO.^{45–48}

Regarding the NO₂RR selectivity, Nb–NiO exhibits fairly low Faradaic efficiencies (FEs) for H₂, NH₂OH, and N₂H₄ by-products relative to FENH₃ (Figure S14), confirming a high NO₂RR selectivity of Nb–NiO toward the NH₃ generation. This finding can be further confirmed by the time-dependent NO₂RR electrolysis (Figure S15), which shows a considerably decreased NO₂[−]–N concentration coupled with a significantly increased NH₃–N concentration as the electrolysis time increases. As a comparison, we evaluate the NO₂RR performance of pristine NiO (Figure 3E), which exhibits much lower NO₂RR activity and selectivity than Nb–NiO. Specifically, Nb–NiO outperforms pristine NiO by 2.3 and 1.3 times in NH₃ yield rate and FENH₃ at −0.6 V, respectively. Besides, Nb–NiO displays a higher electrochemical active surface area (ECSA, Figure S16) than NiO, while the catalyst performance normalized by ECSA (Figure S17) exhibits the same trend with Figure 3E, suggesting the high intrinsic activity of Nb–NiO toward the NO₂RR. As for the electrocatalytic stability of Nb–NiO, slight changes in NH₃ yield rates and FENH₃ over six consecutive cycles can be seen, indicating an excellent cycling stability of Nb–NiO (Figure 3F). The long-term chronoamperometric experiment shows a negligible decline in current density and calculated FENH₃ over 12 h continuous electrolysis (Figure 3G), substantiating the excellent long-term durability of Nb–NiO.^{49–51} After stability tests, Nb–NiO retains its original phase, morphology, and coordination structure (Figure S18), evidencing the high structural stability of Nb–NiO.^{52–54}

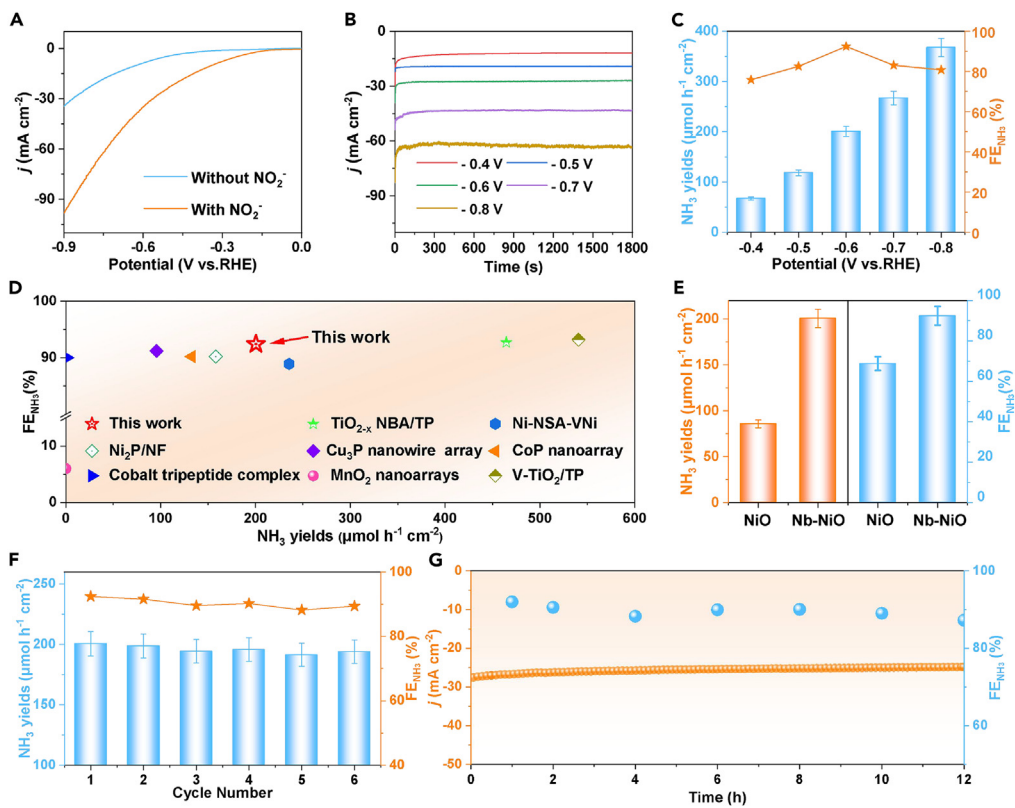


Figure 3. Electrochemical NO_2RR tests

(A) LSV curves of Nb–NiO in various electrolytes.

(B and C) (B) Chronoamperometry test of Nb–NiO at different potentials after 0.5 h electrolysis and (C) obtained NH_3 yield rates and FE_{NH_3} .

(D) Comparison of NH_3 yield rates and FENH_3 between Nb–NiO and reported NO_2RR catalysts.

(E) Comparison of the NO_2RR performance between NiO and Nb–NiO at -0.6 V.

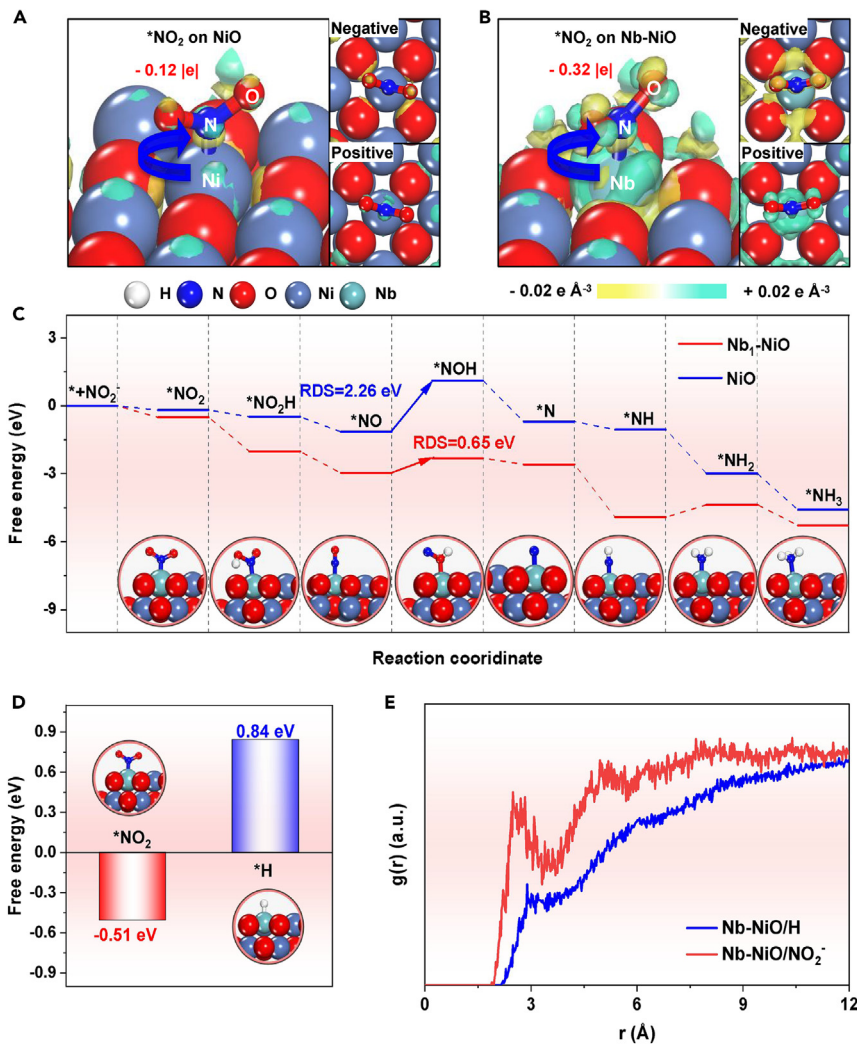
(F and G) (F) Cycling and (G) long-term stability tests of Nb–NiO at -0.6 V.

Theoretical calculations are conducted to elucidate the mechanism for the Nb-doping-induced enhanced NO_2RR performance of Nb–NiO. Upon the NO_2^- adsorption on Nb–NiO (Figure S19), the electron-deficient Nb dopant, as previously determined in Figure 2E, can serve as Lewis acid site to favorably absorb Lewis base NO_2^- , resulting in enhanced NO_2^- activation and N=O bond dissociation.^{55–58} Charge density difference analysis (Figures 4A and 4B) reveals a remarkable Nb– $^*\text{NO}_2$ electronic coupling where Nb dopant donates $-0.32|\text{e}|$ to $^*\text{NO}_2$, in stark contrast to $-0.12|\text{e}|$ for Ni–to– $^*\text{NO}_2$ charge transfer. In addition, the free energy diagram (Figure 4C; Figure S20) presents that both Nb dopant of Nb–NiO and Ni site of NiO exhibit the same rate determining step (RDS) of $^*\text{NO} \rightarrow ^*\text{NHO}$.⁵⁹ Nonetheless, Nb dopant exhibits a much reduced RDS energy barrier compared to Ni site (-2.26 eV). Besides, Nb dopant presents much lower free energies of all protonation intermediates than Ni site. Both findings demonstrate that Lewis acid Nb dopant serve as active site to significantly enhance the protonation energetics to boost the NO_2^- –to– NH_3 conversion process on Nb–NiO.

Considering that HER is the main competing reaction of NO_2RR ,⁶⁰ the HER activity of NO_2RR -active Nb-dopant site is further investigated. As displayed in Figure 4D, the binding free energy of $^*\text{H}$ on Nb dopant of Nb–NiO is calculated as 0.84 eV, which is much positive than that of $^*\text{NO}_2$ (-0.51 eV), confirming an unfavorable HER performance of Nb–NiO, which is attributed to the Lewis acidity of Nb dopant capable of repelling the binding of positively charged H. Additionally, molecular dynamics (MD) simulations (Figure 4E) reveal that the snapshot after simulation (Figure S21) shows the aggregation of evident NO_2^- on Nb–NiO, and the calculated radial distribution function (RDF) curves (Figure 4E) present a more intense Nb–NiO/ $^*\text{NO}_2^-$ interaction compared to Nb–NiO/ $^*\text{H}$ interaction,^{61–63} further corroborating that Nb–NiO is able to selectively adsorb NO_2^- and suppress H coverage, thus facilitating the boosted NO_2RR and inhibited HER. These theoretical results reveal that the Lewis acid Nb dopant of Nb–NiO plays a crucial role in enhancing the efficient adsorption and activation of NO_2^- , boosting the protonation energetics and suppressing the HER, eventually leading to the high catalytic activity and selectivity of Nb–NiO for the NO_2RR .

Conclusion

Nb–NiO has been proved to be an efficient and robust NO_2RR catalyst. Theoretical computations suggest that the enhanced NO_2RR performance of Nb–NiO originates from the key role of Lewis acid Nb dopant in suppressing the HER and enhancing NO_2^- activation and

**Figure 4. Theoretical analysis**(A and B) Charge density difference plots of $^*\text{NO}_2$ on (A) NiO and (B) Nb-NiO. Yellow: charge accumulation, cyan: charge depletion.(C) Free energy profiles of NO₂RR process on NiO and Nb-NiO.(D) Free energies of absorbed H and NO_2^- on Nb-dopant site of Nb-NiO.(E) RDF curves of the interactions between Nb-dopant and NO_2^-/H^+ .

protonation. This work not only offers an in-depth understanding of the Lewis acid dopant-catalyzed NO₂RR mechanism but also implies the great potential of constructing Lewis acid dopants in catalysts to achieve exceptional NO_2^- electroreduction and beyond.

STAR★METHODS

Detailed methods are provided in the online version of this paper and include the following:

- KEY RESOURCES TABLE
- RESOURCE AVAILABILITY
 - Lead contact
 - Materials availability
 - Data and code availability
- METHOD DETAILS
 - Synthesis of Nb-NiO
 - Electrochemical experiments
 - Characterizations

SUPPLEMENTAL INFORMATION

Supplemental information can be found online at <https://doi.org/10.1016/j.isci.2023.107944>.

ACKNOWLEDGMENTS

This work is supported by The First Batch of University Level Scientific Research Projects of Hebei North University in 2022 (E2022405002).

AUTHOR CONTRIBUTIONS

Ying Zhang: Investigation, Writing-original draft. Yuying Wan: Investigation. Xiaoxu Liu: Software, Investigation. Kai Chen: Investigation.

DECLARATION OF INTERESTS

The authors declare no competing interests.

Received: July 6, 2023

Revised: July 20, 2023

Accepted: September 14, 2023

Published: September 19, 2023

REFERENCES

1. Liang, J., Li, Z., Zhang, L., He, X., Luo, Y., Zheng, D., Wang, Y., Li, T., Yan, H., Ying, B., et al. (2023). Advances in ammonia electrocatalysis from ambient nitrate/nitrite reduction. *Chem.* 9, 1768–1827.
2. Liang, J., Liu, Q., Alshehri, A.A., and Sun, X. (2022). Recent advances in nanostructured heterogeneous catalysts for N-cycle electrocatalysis. *Nano Res. Energy* 1, e9120010.
3. Qi, D., Lv, F., Wei, T., Jin, M., Meng, G., Zhang, S., Liu, Q., Liu, W., Ma, D., Hamdy, M.S., et al. (2022). High-efficiency electrocatalytic NO reduction to NH₃ by nanoporous VN. *Nano Res. Energy* 1, e9120022.
4. Liu, Q., Xu, T., Luo, Y., Kong, Q., Li, T., Lu, S., Alshehri, A.A., Alzahrani, K.A., and Sun, X. (2021). Recent advances in strategies for highly selective electrocatalytic N₂ reduction toward ambient NH₃ synthesis. *Curr. Opin. Electrochem.* 29, 100766.
5. Luo, Y., Shen, P., Li, X., Guo, Y., and Chu, K. (2022). Sulfur-deficient Bi₂S_{3-x} synergistically coupling Ti₃C₂T_x-MXene for boosting electrocatalytic N₂ reduction to NH₃. *Adv. Energy Mater.* 12, 2103022.
6. Chu, K., Luo, Y., Shen, P., Li, X., Li, Q., and Guo, Y. (2022). Unveiling the synergy of O-vacancy and heterostructure over MoO_{3-x}/MXene for N₂ electroreduction to NH₃. *Adv. Energy Mater.* 12, 2103022.
7. Qing, G., Ghazfar, R., Jackowski, S.T., Habibzadeh, F., Ashtiani, M.M., Chen, C.-P., Smith, M.R., and Hamann, T.W. (2020). Recent advances and challenges of electrocatalytic N₂ reduction to ammonia. *Chem. Rev.* 120, 5437–5516.
8. Li, X., Shen, P., Luo, Y., Li, Y., Guo, Y., Zhang, H., and Chu, K. (2022). PdFe single-atom alloy metathene for N₂ electroreduction. *Angew. Chem. Int. Ed. Engl.* 61, e202205923.
9. Chen, Y., Chen, C., Cao, X., Wang, Z., Zhang, N., and Liu, T. (2023). Recent advances in defect and interface engineering for electroreduction of CO₂ and N₂. *Acta Phys. Chim. Sin.* 39, 2212053.
10. Chu, K., Li, X., Li, Q., Guo, Y., and Zhang, H. (2021). Synergistic enhancement of electrocatalytic nitrogen reduction over boron nitride quantum dots decorated Nb₂CT_x-MXene. *Small* 17, 2102363.
11. Wang, H., Zhang, F., Jin, M., Zhao, D., Fan, X., Li, Z., Luo, Y., Zheng, D., Li, T., Wang, Y., et al. (2023). V-doped TiO₂ nanobelt array for high-efficiency electrocatalytic nitrite reduction to ammonia. *Mater. Today Phys.* 30, 100944.
12. He, X., Li, Z., Yao, J., Dong, K., Li, X., Hu, L., Sun, S., Cai, Z., Zheng, D., Luo, Y., et al. (2023). High-efficiency electrocatalytic nitrite reduction toward ammonia synthesis on CoP@TiO₂ nanoribbon array. *iScience* 26, 107100.
13. He, X., Hu, L., Xie, L., Li, Z., Chen, J., Li, X., Li, J., Zhang, L., Fang, X., Zheng, D., et al. (2023). Ambient ammonia synthesis via nitrite electroreduction over NiS₂ nanoparticles-decorated TiO₂ nanoribbon array. *J. Colloid Interface Sci.* 634, 86–92.
14. Cai, Z., Zhao, D., Fan, X., Zhang, L., Liang, J., Li, Z., Li, J., Luo, Y., Zheng, D., Wang, Y., et al. (2023). Rational construction of heterostructured Cu₃P@TiO₂ nanoarray for high-efficiency electrochemical nitrite reduction to ammonia. *Small* 19, 2300620.
15. Zhu, X., Fan, X., Lin, H., Li, S., Zhai, Q., Jiang, Y., and Chen, Y. (2023). Highly efficient electroenzymatic cascade reduction reaction for the conversion of nitrite to ammonia. *Adv. Energy Mater.* 13, 2300669.
16. Zhang, Y., Wang, Y., Han, L., Wang, S., Cui, T., Yan, Y., Xu, M., Duan, H., Kuang, Y., and Sun, X. (2023). Nitrite electroreduction to ammonia promoted by molecular carbon dioxide with near-unity Faradaic efficiency. *Angew. Chem. Int. Ed. Engl.* 62, e202213711.
17. Liu, Q., Wen, G., Zhao, D., Xie, L., Sun, S., Zhang, L., Luo, Y., Ali Alshehri, A., Hamdy, M.S., Kong, Q., and Sun, X. (2022). Nitrite reduction over Ag nanoarray electrocatalyst for ammonia synthesis. *J. Colloid Interface Sci.* 623, 513–519.
18. Liu, Q., Liu, Q., Xie, L., Yue, L., Li, T., Luo, Y., Li, N., Tang, B., Yu, L., and Sun, X. (2022). A 3D FeOOH nanotube array: an efficient catalyst for ammonia electrocatalysis by nitrite reduction. *Chem. Commun.* 58, 5160–5163.
19. Li, S., Liang, J., Wei, P., Liu, Q., Xie, L., Luo, Y., and Sun, X. (2022). ITO@TiO₂ nanoarray: An efficient and robust nitrite reduction reaction electrocatalyst toward NH₃ production under ambient conditions. *eScience* 2, 382–388.
20. Lang, R., Du, X., Huang, Y., Jiang, X., Zhang, Q., Guo, Y., Liu, K., Qiao, B., Wang, A., and Zhang, T. (2020). Single-atom catalysts based on the metal–oxide interaction. *Chem. Rev.* 120, 11986–12043.
21. Lee, J., Kumar, A., Kim, M.G., Yang, T., Shao, X., Liu, X., Liu, Y., Hong, Y., Jadhav, A.R., Liang, M., et al. (2021). Single-metal-atom dopants increase the Lewis acidity of metal oxides and promote nitrogen fixation. *ACS Energy Lett.* 6, 4299–4308.
22. Chang, Q.-Y., Wang, K.-Q., Sui, Z.-J., Zhou, X.-G., Chen, D., Yuan, W.-K., and Zhu, Y.-A. (2021). Rational design of single-atom-doped Ga₂O₃ catalysts for propane dehydrogenation: breaking through volcano plot by Lewis acid-base interactions. *ACS Catal.* 11, 5135–5147.
23. Zhang, J., Zhou, R.-J., Chang, Q.-Y., Sui, Z.-J., Zhou, X.-G., Chen, D., and Zhu, Y.-A. (2021). Tailoring catalytic properties of V₂O₃ to propane dehydrogenation through single-atom doping: A DFT study. *Catal. Today* 368, 46–57.
24. Ma, F., Chang, Q.-Y., Yin, Q., Sui, Z.-J., Zhou, X.-G., Chen, D., and Zhu, Y.-A. (2020). Rational screening of single-atom-doped ZnO catalysts for propane dehydrogenation from microkinetic analysis. *Catal. Sci. Technol.* 10, 4938–4951.
25. Chu, K., Liu, Y.-p., Li, Y.-b., Guo, Y.-l., Tian, Y., and Zhang, H. (2020). Multi-functional Mo-doping in MnO₂ nanoflowers toward efficient and robust electrocatalytic nitrogen fixation. *Appl. Catal.*, B 264, 118525.
26. Huang, H., Gong, F., Wang, Y., Wang, H., Wu, X., Lu, W., Zhao, R., Chen, H., Shi, X., Asiri, A.M., et al. (2019). Mn₃O₄ nanoparticles@reduced graphene oxide composite: An efficient electrocatalyst for artificial N₂ fixation to NH₃ at ambient conditions. *Nano Res.* 12, 1093–1098.
27. Zhang, Y., Qiu, W., Ma, Y., Luo, Y., Tian, Z., Cui, G., Xie, F., Chen, L., Li, T., and Sun, X. (2018). High-performance electrohydrogenation of N₂ to NH₃ catalyzed by multishelled hollow Cr₂O₃ microspheres under ambient conditions. *ACS Catal.* 8, 8540–8544.

28. Zhang, L., Ji, X., Ren, X., Ma, Y., Shi, X., Tian, Z., Asiri, A.M., Chen, L., Tang, B., and Sun, X. (2018). Electrochemical ammonia synthesis via nitrogen reduction reaction on a MoS₂ catalyst: theoretical and experimental studies. *Adv. Mater.* 30, 1800191.
29. Zhu, L., Zhong, Z., Xue, J., Xu, Y., Wang, C., and Wang, L. (2018). NH₃-SCR performance and the resistance to SO₂ for Nb doped vanadium based catalyst at low temperatures. *J. Environ. Sci.* 65, 306–316.
30. Kong, W., Liu, Z., Han, J., Xia, L., Wang, Y., Liu, Q., Shi, X., Wu, Y., Xu, Y., and Sun, X. (2019). Ambient electrochemical N₂-to-NH₃ fixation enabled by Nb₂O₅ nanowire array. *Inorg. Chem. Front.* 6, 423–427.
31. Huang, L., Wu, J., Han, P., Al-Enizi, A.M., Almutairi, T.M., Zhang, L., and Zheng, G. (2019). NbO₂ electrocatalyst toward 32% Faradaic efficiency for N₂ fixation. *Small Methods* 3, 1800386.
32. Han, J., Liu, Z., Ma, Y., Cui, G., Xie, F., Wang, F., Wu, Y., Gao, S., Xu, Y., and Sun, X. (2018). Ambient N₂ fixation to NH₃ at ambient conditions: Using Nb₂O₅ nanofiber as a high-performance electrocatalyst. *Nano Energy* 52, 264–270.
33. Wang, X., Wang, J., Li, Y., and Chu, K. (2019). Nitrogen-doped NiO nanosheet array for boosted electrocatalytic N₂ reduction. *ChemCatChem* 11, 4529–4536.
34. Chen, K., Zhang, Y., Xiang, J., Zhao, X., Li, X., and Chu, K. (2023). p-block antimony single-atom catalysts for nitric oxide electroreduction to ammonia. *ACS Energy Lett.* 8, 1281–1288.
35. Wang, J., Cao, G., Duan, R., Li, X., and Li, X. (2023). Advances in single metal atom catalysts enhancing kinetics of sulfur cathode. *Acta Phys. Chim. Sin.* 39, 2212005.
36. Chen, K., Wang, J., Zhang, H., Ma, D., and Chu, K. (2023). Self-tandem electrocatalytic NO reduction to NH₃ on a W single-atom catalyst. *Nano Lett.* 23, 1735–1742.
37. Chen, K., Wang, J., Kang, J., Lu, X., Zhao, X., and Chu, K. (2023). Atomically Fe-doped MoS_{2-x} with Fe-Mo dual sites for efficient electrocatalytic NO reduction to NH₃. *Appl. Catal.*, B 324, 122241.
38. Zhang, N., Zhang, G., Shen, P., Zhang, H., Ma, D., and Chu, K. (2023). Lewis acid Fe-V pairs promote nitrate electroreduction to ammonia. *Adv. Funct. Mater.* 33, 2211537.
39. Zhang, G., Zhang, N., Chen, K., Zhao, X., and Chu, K. (2023). Atomically Mo-doped SnO_{2-x} for efficient nitrate electroreduction to ammonia. *J. Colloid Interface Sci.* 649, 724–730.
40. Li, X., Chen, K., Lu, X., Ma, D., and Chu, K. (2023). Atomically dispersed Co catalyst for electrocatalytic NO reduction to NH₃. *Chem. Eng. J.* 454, 140333.
41. Xu, Y., Wen, Y., Ren, T., Yu, H., Deng, K., Wang, Z., Li, X., Wang, L., and Wang, H. (2023). Engineering the surface chemical microenvironment over CuO nanowire arrays by polyaniline modification for efficient ammonia electrosynthesis from nitrate. *Appl. Catal.*, B 320, 121981.
42. Ren, T., Yu, Z., Yu, H., Deng, K., Wang, Z., Li, X., Wang, H., Wang, L., and Xu, Y. (2023). Sustainable ammonia electrosynthesis from nitrate wastewater coupled to electrocatalytic upcycling of polyethylene terephthalate plastic waste. *ACS Nano* 17, 12422–12432.
43. Ren, T., Yu, Z., Yu, H., Deng, K., Wang, Z., Li, X., Wang, H., Wang, L., and Xu, Y. (2022). Interfacial polarization in metal-organic framework reconstructed Cu/Pd/CuO_x multi-phase heterostructures for electrocatalytic nitrate reduction to ammonia. *Appl. Catal.*, B 318, 121805.
44. Ren, T., Sheng, Y., Wang, M., Ren, K., Wang, L., and Xu, Y. (2022). Recent advances of Cu-based materials for electrochemical nitrate reduction to ammonia. *Chinese J. Struct. Chem.* 41, 2212089–2212106.
45. Wang, G., Zhang, Y., Chen, K., Guo, Y., and Chu, K. (2023). PdP₂ nanoparticles on reduced graphene oxide: a catalyst for the electrocatalytic reduction of nitrate to ammonia. *Inorg. Chem.* 62, 6570–6575.
46. Li, X., Shen, P., Li, X., Ma, D., and Chu, K. (2023). Sub-nm RuO_x clusters on Pd metallene for synergistically enhanced nitrate electroreduction to ammonia. *ACS Nano* 17, 1081–1090.
47. Chen, K., Wang, F., Lu, X., Li, Y., and Chu, K. (2023). Atomically dispersed W₁-O₃ bonded on Pd metallene for cascade NO electroreduction to NH₃. *ACS Catal.* 13, 9550–9557.
48. Zhang, G., Li, X., Chen, K., Guo, Y., Ma, D., and Chu, K. (2023). Tandem electrocatalytic nitrate reduction to ammonia on MBenes. *Angew. Chem. Int. Ed. Engl.* 62, e202300054.
49. Zhang, Q., Lian, K., Liu, Q., Qi, G., Zhang, S., Luo, J., and Liu, X. (2023). High entropy alloy nanoparticles as efficient catalysts for alkaline overall seawater splitting and Zn-air batteries. *J. Colloid Interface Sci.* 646, 844–854.
50. Zhang, H., Wei, T., Qiu, Y., Zhang, S., Liu, Q., Hu, G., Luo, J., and Liu, X. (2023). Recent progress in metal phosphorous chalcogenides: potential high-performance electrocatalysts. *Small* 19, 2207249.
51. Wei, T., Liu, W., Zhang, S., Liu, Q., Luo, J., and Liu, X. (2023). A dual-functional Bi-doped Co₃O₄ nanosheet array towards high efficiency 5-hydroxymethylfurfural oxidation and hydrogen production. *Chem. Commun.* 59, 442–445.
52. Hu, P., Hu, S., Du, H., Liu, Q., Guo, H., Ma, K., and Li, T. (2023). Efficient electrocatalytic reduction of nitrate to ammonia over fibrous SmCoO₃ under ambient conditions. *Chem. Commun.* 59, 5697–5700.
53. Du, H., Guo, H., Wang, K., Du, X., Beshiwork, B.A., Sun, S., Luo, Y., Liu, Q., Li, T., and Sun, X. (2023). Durable electrocatalytic reduction of nitrate to ammonia over defective pseudobrookite Fe₂TiO₅ nanofibers with abundant oxygen vacancies. *Angew. Chem. Int. Ed. Engl.* 62, e202215782.
54. Dong, S., Niu, A., Wang, K., Hu, P., Guo, H., Sun, S., Luo, Y., Liu, Q., Sun, X., and Li, T. (2023). Modulation of oxygen vacancy and zero-valent zinc in ZnCr₂O₄ nanofibers by enriching zinc for efficient nitrate reduction. *Appl. Catal.*, B 333, 122772.
55. Chen, K., Ma, Z., Li, X., Kang, J., Ma, D., and Chu, K. (2023). Single-atom Bi alloyed Pd metallene for nitrate electroreduction to ammonia. *Adv. Funct. Mater.* 33, 2209890.
56. Zhang, Y., Xiang, J., Chen, K., Guo, Y., Ma, D., and Chu, K. (2023). Palladium metallene for nitric oxide electroreduction to ammonia. *Chem. Commun.* 59, 8961–8964.
57. Wang, G., Shen, P., Chen, K., Guo, Y., Zhao, X., and Chu, K. (2023). Rare-earth La-doped VS_{2-x} for electrochemical nitrate reduction to ammonia. *Inorg. Chem. Front.* 10, 2014–2021.
58. Chen, K., Zhang, N., Wang, F., Kang, J., and Chu, K. (2023). Main-group indium single-atom catalysts for efficient electrocatalytic NO reduction to NH₃. *J. Mater. Chem. A* 11, 6814–6819.
59. Wang, J., Liang, J., Liu, P., Yan, Z., Cui, L., Yue, L., Zhang, L., Ren, Y., Li, T., Luo, Y., et al. (2022). Biomass Juncus derived carbon decorated with cobalt nanoparticles enables high-efficiency ammonia electrosynthesis by nitrite reduction. *J. Mater. Chem. A* 10, 2842–2848.
60. Zhang, X., Wang, Y., Wang, Y., Guo, Y., Xie, X., Yu, Y., and Zhang, B. (2022). Recent advances in electrocatalytic nitrite reduction. *Chem. Commun.* 58, 2777–2787.
61. Zhang, G., Wan, Y., Zhao, H., Guo, Y., and Chu, K. (2023). A metal-free catalyst for electrocatalytic NO reduction to NH₃. *Dalton Trans.* 52, 6248–6253.
62. Chen, K., Zhang, Y., Du, W., Guo, Y., and Chu, K. (2023). Atomically-isolated and unsaturated Sb sites created on Sb₂S₃ for highly selective NO electroreduction to NH₃. *Inorg. Chem. Front.* 10, 2708–2715.
63. Chen, K., Wang, G., Guo, Y., Ma, D., and Chu, K. (2023). Iridium single-atom catalyst for highly efficient NO electroreduction to NH₃. *Nano Res.* 16, 8737–8742.

STAR★METHODS

KEY RESOURCES TABLE

REAGENT or RESOURCE	SOURCE	IDENTIFIER
Chemicals, peptides, and recombinant proteins		
NaNO ₂	Aladdin Co., Ltd.	7632-00-0
NaClO	Aladdin Co., Ltd.	7681-52-9
C ₅ FeN ₆ Na ₂ O·2H ₂ O	Aladdin Co., Ltd.	13755-38-9
H ₂ O ₂	Beijing Chemical Corporation	7722-84-1
H ₂ SO ₄	Beijing Chemical Corporation	7664-93-9
HCl	Beijing Chemical Corporation	7647-01-0
C ₂ H ₅ OH	Beijing Chemical Corporation	64-17-5
C ₁₀ H ₅ NbO ₂₀	McLean Co., Ltd.	21348-59-4
Ni(NO ₃) ₂ ·6H ₂ O	Sinopharm Chemical Reagent Co., Ltd.	13478-00-7

RESOURCE AVAILABILITY

Lead contact

Further information and requests for resources should be directed to and will be fulfilled by the lead contact, Dr. Ke Chu (chuk630@mail.izjtu.cn).

Materials availability

This study did not generate new unique reagents. All chemicals were obtained from commercial resources and used as received.

Data and code availability

Data reported in this paper will be shared by the [lead contact](#) upon reasonable request.

All original code is available in this paper's [supplemental information](#).

Any additional information required to reanalyze the data reported in this paper is available from the [lead contact](#) upon reasonable request.

METHOD DETAILS

Synthesis of Nb–NiO

0.3 g Ni(NO₃)₂·6H₂O and 0.32 g C₁₀H₅NbO₂₀ were dispersed in 30 mL ethanol solution under stirring to form a transparent solution. Afterward, the solution was transferred into a 50 mL autoclave. After treatment at 150°C for 6 h, the light green precipitates were collected by centrifuging, washed with deionized water/ethanol and dried under vacuum overnight. The obtained precipitates were ground in an agate mortar and then transferred to a muffle furnace for calcination at 300°C for 4 h to obtain Nb–NiO. Pristine NiO was prepared by the same method as Nb–NiO by without addition of C₁₀H₅NbO₂₀.

Electrochemical experiments

Electrochemical measurements were investigated with a CHI-760E electrochemical workstation using a conventional three-electrode cell. Nb–NiO coated on carbon cloth (1 × 1 cm², 0.5 mg cm⁻²) was used as the working electrode, Ag/AgCl (saturated KCl) electrode was used as the reference electrode, and Pt foil was used as the counter electrode. All potentials were referenced to reversible hydrogen electrode (RHE) by following equation: $E(\text{V vs. RHE}) = E(\text{V vs. Ag/AgCl}) + 0.198\text{V} + 0.059 \times \text{pH}$. The NO₂RR measurements were carried out in 0.5 M Na₂SO₄ + 0.1 M NaNO₂ electrolyte using an H-type two-compartment electrochemical cell separated by a Nafion 211 membrane. After each chronoamperometry test for 0.5 h, the produced NH₃ and other possible by-product (N₂H₄) were analyzed by various colorimetric methods using UV-vis absorbance spectrophotometer (MAPADA P5), while the gas products (H₂, NH₂OH) were analyzed by gas chromatography (Shimadzu GC2010). The detailed determination procedures are given in our previous publication.⁴⁶

Faradaic efficiency (FE) of NH₃ generation was calculated by the following equation:

$$FE = (6 \times F \times c \times V) / (17 \times Q) \times 100\% \quad (\text{Equation 1})$$

NH₃ yield rate is calculated using the following equation:

$$NH_3 \text{ yield rate} = (c \times V) / (17 \times t \times A) \quad (\text{Equation 2})$$

where c ($\mu\text{g mL}^{-1}$) is the measured NH_3 concentration, V (mL) is the volume of the electrolyte in the cathode chamber (35 mL), t (s) is the electrolysis time, A (cm^{-2}) is the surface area of CC ($1 \times 1 \text{ cm}^2$), F (96500 C mol^{-1}) is the Faraday constant, Q (C) is the total quantity of applied electricity.

Characterizations

X-ray diffraction (XRD) was conducted on a Rigaku D/max 2400 diffractometer. Scanning electron microscopy (SEM) was carried out on a ZEISS GeminiSEM-500 microscope. Transmission electron microscopy (TEM) and high-resolution transmission electron microscopy (HRTEM) were performed on a Tecnai G² F20 microscope at an acceleration voltage of 200 kV.